Astronomy & Astrophysics manuscript no. hackman_mhd2zdi_subm ©ESO 2023
June 14, 2023

From convective stellar dynamo simulations to Zeeman-Doppler images

T. Hackman[1], O. Kochukhov[2], M. Viviani[3], J. Warnecke[4], M.J. Korpi-Lagg[5,4,6], and J.J. Lehtinen[7,1]

[1] Department of Physics, P.O. Box 64, FI-00014 University of Helsinki, Finland
e-mail: `thomas.hackman@helsinki.fi`
[2] Department of Physics and Astronomy, Uppsala University, Box 516, S-75120 Uppsala, Sweden
[3] Wish s.r.l, Via Venezia 24, 87036 Rende (CS), Italy
[4] Max-Planck-Institut für Sonnensystemforschung, Justus-von-Liebig-Weg 3, D-37077 Göttingen, Germany
[5] Department of Computer Science, Aalto University, PO Box 15400, FI-00076 Espoo, Finland
[6] Nordita, KTH Royal Institute of Technology & Stockholm University, Hannes Alfvéns väg 12, Stockholm, SE-11419, Sweden
[7] Finnish Centre for Astronomy with ESO (FINCA), University of Turku, Vesilinnantie 5, FI-20014 University of Turku, Finland

Received ; accepted

ABSTRACT

Context. Zeeman-Doppler imaging (ZDI) is used to reconstruct the surface magnetic field of late-type stars from high resolution spectropolarimetric observations. The results are usually described in terms of characteristics of the field topology, i.e. poloidality vs. toroidality and axi-symmetry vs. non-axisymmetry in addition to the field strength.

Aims. In this study we want to test how well these characteristics are preserved when applying the ZDI method on simulated data. We are particularly interested in how accurately the field topology is preserved and to what extent stellar parameters, i.e. the projected rotation velocity and rotation axis inclination, influence the reconstruction.

Methods. For the test we use published magnetic field vector data from direct numerical magnetohydrodynamic simulations taken near the surface of the simulation domain. These simulations have variable rotation rates, and hence represent different levels of activity, of an otherwise Sun-like setup with a convective envelope of solar thickness. Our ZDI reconstruction is based on spherical harmonics expansion. By comparing the original values to those of the reconstructed images, we study the ability to reconstruct the surface magnetic field in terms of various characteristics of the field.

Results. In general the ZDI method works as expected. The main large-scale features are reasonably well recovered, but the strength of the recovered magnetic field is just a fraction of the original input. The quality of the reconstruction shows clear correlations with the data quality. Furthermore, there are some spurious dependencies between stellar parameters and the characteristics of the field.

Conclusions. Our study uncovers some limits of ZDI. Firstly, the recovered field strength will generally be lower than the "real" value as smaller structures with opposite polarities will be blurred in the inversion. This is also seen in the relative distribution of magnetic energy in terms of the angular degree ℓ. Secondly, the axi-symmetry is overestimated. The poloidality vs. toroidality is better recovered. The reconstruction works better for a stronger field and faster rotation velocity. Still, the ZDI method works surprisingly well even for a weaker field and slow rotation, provided the data has a high signal-to-noise and good rotation phase coverage.

Key words. Methods: numerical – Magnetohydrodynamics – Dynamo – Stars: activity – magnetic fields – imaging

1. Introduction

Zeeman-Doppler Imaging (ZDI, Brown et al. 1991; Kochukhov 2016) is a powerful method to reconstruct surface magnetic field maps of late-type stars. In ZDI high-resolution spectropolarimetric observations (Stokes IVQU, Stokes IV or just Stokes V) are used as input data. The observations are normally limited to only Stokes IV, as the linear polarisation signal is usually too weak to measure within reasonable exposure times. The solution is retrieved as magnetic field vector component maps presenting the surface radial B^r, meridional B^θ and azimuthal B^ϕ components (see e.g. Hackman et al. 2016).

Besides estimating the strength of the magnetic field, the topology is an important characteristic. Usually the field topology is described in terms of fractions of poloidal vs. toroidal and axi-symmetric vs. non-axisymmetric field energy. These are straightforward to calculate when the field solution is derived in terms of a spherical harmonics expansion (see e.g. Donati et al. 2006). The characteristics are used to illustrate the strength and topologies of stellar magnetic fields as functions of stellar parameters (e.g. Rossby number, age and spectral class) in plots commonly referred to as “confusograms” (see e.g. Donati et al. 2008). In the case of a series of ZDI:s from a particular star, the characteristics can be used to illustrate the changes in the magnetic field topology possibly related to activity cycles (see e.g. Kochukhov et al. 2013).

Testing the ZDI method is challenging, since the Sun is the only late-type star for which we can directly resolve the surface magnetic field vector. The study by Vidotto (2016) shows what we could expect in terms of ZDI by observing the Sun as a star. A synoptic map of the solar surface magnetic vector field (Carrington Rotation CR2109), was used to reconstruct the surface field with spherical harmonics decomposition using different values for the highest angular degree ($\ell_{\max} = 5$ and $\ell_{\max} = 150$). With $\ell_{\max} = 5$, which corresponds to the typical value used for ZDI inversions of slowly rotating active stars, most of the magnetic field remains undetected. Furthermore, the fractional strengths of the different field components is strongly biased towards B^r. The cumulative fraction of poloidal field energy is constantly over 0.9, showing some fluctuations at the lowest degrees ($\ell < 10$), reaching a local maximum of approx. 0.97 around $\ell \approx 15$ and then smoothly settling towards 0.91 at $\ell = 150$.

Another approach is to apply ZDI on stellar magnetic fields calculated from simulations. Lehmann et al. (2019) used 3D global magnetic field simulations to study how well the ZDI method was able to reconstruct the magnetic field at the surface. In these simulations (Lehmann et al. 2018; Gibb et al. 2016) a surface flux-transport model was adopted, in which case only the surface evolution of the large-scale magnetic field was solved for. Starspots emerged on the surface at a rate which is a free parameter of the model, as was also the rotation rate and differential rotation profile of the star. Lehmann et al. (2019) chose models with one, three and five times the solar angular rotation velocity to mimic the Sun and more active stars.

In the present study, in contrast, we use direct numerical simulations of stellar dynamos (Viviani et al. 2018, 2019). These models solve the full magnetohydrodynamic equations in the stellar convection zone self-consistently without relying on a surface flux transport approach, hence also producing strong magnetic fields on small scales. In the full MHD approach, the differential rotation profile emerges as a solution to the Navier-Stokes equation, while the only input parameter is the rotation rate (or Coriolis number).

The rotation profiles of other stars than the Sun are largely unknown. Thus, one may argue that the direct numerical simulations, containing less free parameters and with differential rotation emerging as a natural solution to the equations, would give better representations of real stars. Furthermore, also the meridional circulation is part of the solution and varies with the level of stellar activity, whereas in the simulations used by Lehmann et al. (2019) it was kept constant. In our convective dynamo simulations, the differential rotation together with the turbulent convection generates the magnetic field solution self-consistently and is not prescribed by a parameterized flux emergence model. Also, compared with their work, the simulations we use cover a larger parameter regime in terms of rotation and activity. Moreover, because of the their setup, their solution will be dominated by the $m = 0$ mode, whereas our selected simulations contain cases with both $m = 0$ and $m = 1$ domination.

Our main focus is to learn how well the magnetic field topology is preserved in the ZDI inversion using Stokes V spectra calculated from a simulated stellar magnetic field as realistic as possible. We use three simulations in our study. For each simulation we apply a set of different projected rotation velocities $v \sin i$. For one simulation we also test the effect of different rotation axis inclinations i. We also want to roughly estimate what level of observation data quality (signal-to-noise ratio, rotation phase coverage) is needed for ZDI in different cases. Contrary to Lehmann et al. (2019) we do not test different descriptions of the magnetic field, in terms of the relations between the spherical harmonics coefficients $\alpha_{\ell,m}$, $\beta_{\ell,m}$ and $\gamma_{\ell,m}$. Instead we only use the description of divergence free field with maximum degrees of freedom (case (iv); Lehmann et al. 2019).

2. Zeeman-Doppler imaging method

The ZDI inversion code used in this study, InversLSD, was introduced by Kochukhov et al. (2014). This code has been successfully applied to a number of active late-type stars (Kochukhov 2015; Hackman et al. 2016; Rosén et al. 2016; Willamo et al. 2022). The code is designed to model least-squares deconvolved (see e.g. Donati et al. 1997, LSD) Stokes IV or IQUV profiles of photospheric absorption lines. Disk-integrated theoretical Stokes parameter spectra are calculated based on pre-tabulated grids of local line profiles computed for a set of continuum brightness values (normalised to 1), magnetic field strengths and orientations, and limb angles. Local line profiles can be computed using full polarised radiative transfer calculations (e.g. Kochukhov et al. 2014; Rosén et al. 2015) or using the analytical Unno-Rachkovsky solution (Landi Degl'Innocenti & Landolfi 2004) obtained under the assumption of Milne-Eddington atmospheres. Here we use the latter approach, which is not relying on the assumption of a weak magnetic field.

A detailed discussion of the method can be found in e.g. Rosén et al. (2016). Of particular relevance for this study is the parameterisation of the stellar surface magnetic field. Both pixel-based specification of the three magnetic field vector components (radial, meridional and azimuthal) and a description of these components in terms of a general harmonic expansion in poloidal and toroidal components are accepted as input formats in InversLSD (see Kochukhov et al. 2014, for details). Here we use the former (pixel-based) approach in the context of the forward calculations to simulate observational data while the latter approach (harmonic parameterisation) is employed for the inversions.

We use the same model to calculate synthetic spectra, and retrieve the inverse solution. Thus systematic errors caused by the approximations in the line calculations become irrelevant. There is, however, another source of systematic errors. The ZDI solution is reconstructed in terms of a spherical harmonics expansion, and thus a maximum angular degree $\ell_{\max}$ has to be set for the inversion. This is discussed further in section 4.

3. Selected simulations and pre-processing

We selected three simulations from the study by Viviani et al. (2018): C1, H^a and L^a. These three models represent a large range of rotation rate and activity and harbour three different and particularly interesting magnetic field solutions.

The Run C1 has the highest rotation rate (1.8 solar), which still produces anti-solar-like differential rotation (i.e. slow equator, fast poles). It has a unique solution of a cyclic axi-symmetric field in the anti-solar differential regime, which was studied in detailed in Viviani et al. (2019). For this run the $m = 0$ (axis-symmetric) magnetic field mode is the strongest mode with cycle period of around 3.3 yrs. The Run H^a has a higher rotation rate (7.8 solar) and exhibits a non-axis-symmetric large-scale magnetic field, where the $m = 1$ mode dominates. This mode is generated by a dynamo wave travelling in the retrograde azimuthal direction. The Run L^a has an even higher rotation rate (23.3 solar) and exhibits a strong $m = 1$ mode, which is two orders of magnitude larger than the $m = 0$ mode. This run shows the feature of a standing azimuthal dynamo wave. From these runs we chose a time point of the time series, where the magnetic field growth had saturated and the properties of the dynamo and the magnetic field configuration did no longer change significantly.

The simulations of Viviani et al. (2018) are based on the setup of Käpylä et al. (2013) using the Pencil Code (Pencil Code Collaboration et al. 2021). The simulation scheme is using finite-differences in spherical coordinates, due to which the grid cell dimensions are decreasing towards the poles. The time step, proportional to the grid cell dimension, for integrating forward in time would correspondingly decrease, leading to unrealistically long computing times. Hence, the simulations leave

Table 1. Parameters and field characteristics for selected simulations. The characteristics are calculated from the pre-processed input data.

Simulation	Grid	Ω $[\Omega_\odot]$	Co	$B_{\rm RMS}$ [kG]	$B^r_{\rm RMS}$ [kG]	$B^\theta_{\rm RMS}$ [kg]	$B^\phi_{\rm RMS}$ [kG]	$B^{\ell\leq20}_{\rm RMS}$ [kG]	$p_{\rm pol}$ [%]	$p^{\ell\leq20}_{\rm pol}$ [%]	$p_{\rm axi}$ [%]	$p^{\ell\leq20}_{\rm axi}$ [%]
C1	144 × 288	1.8	2.8	0.217	0.124	0.105	0.144	0.11	61.5	55.9	11.0	28.2
H^a	256 × 512	7.8	16.1	0.480	0.240	0.262	0.322	0.37	62.5	81.8	2.8	0.6
L^a	256 × 512	23.3	83.4	0.483	0.286	0.311	0.234	0.31	69.5	82.1	2.7	5.4

Notes. Ω is the rotation rate of the simulations in terms of the solar rotation rate $\Omega_\odot$ and Co is the Coriolis number as defined in Viviani et al. (2018).

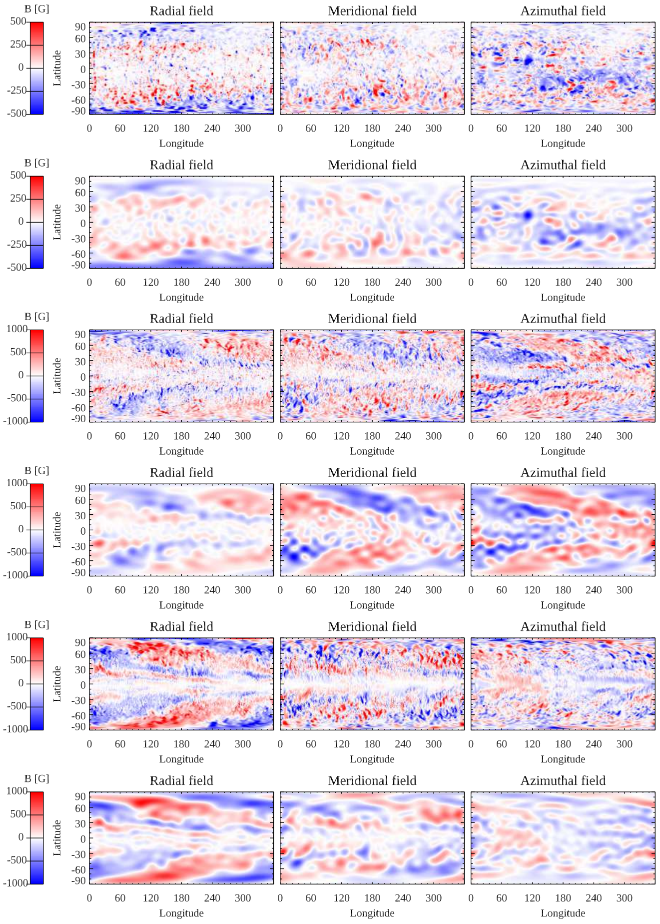

Fig. 1. Input magnetic field data for the ZDI calculations from top to bottom: C1, $\mathrm{C1}_{\ell\leq20}$, H^a, $\mathrm{H}^a_{\ell\leq20}$, L^a and $\mathrm{L}^a_{\ell\leq20}$.

out 15° of latitudes around the poles. Since this does not correspond to the situation in real stars, we artificially stretched the magnetic field data to cover these regions. Furthermore, the simulations do not describe the stellar surface properties correctly. E.g. the density stratification is much lower near the surface than in a Sun-like star, also the magnetic field is set to be purely radial at the $r = R_\star$ surface, where $R_\star$ is the stellar radius. Therefore, we take only the magnetic field data from a slice just below the surface ($r = 0.98R_\star$), where the influence of the boundary conditions is not strong and all magnetic field components are present. The simulations do not provide an absolute scale of the magnetic field strength, as they deal with non-dimensional numbers. They do, however, allow for selecting a unit system, so that the simulated magnetic field strength can be matched with the observed ones. The simulations units are scaled to physical units by assuming that the simulations rotate with 1.8, 7.8 and 23.3 times the solar value, that the density at the bottom of the convection zone is the solar one and the radial extent of the domain is the size of the solar convection zone ($0.3\,R_\star$), see Viviani et al. (2018) for details. To compensate for the missing density stratification near the surface, we scale the surface magnetic field strength down to values comparable to observations, see Table 1.

The geometry of the simulated magnetic field data did not correspond to the input format for the ZDI code. The grid dimensions of the C1 simulated data were 144 × 288, in latitude and longitude, respectively, and for the H^a and L^a 256×512. The data were first down-sampled to half of the grid sizes, and then converted to a Mollweide-type format with 20862 surface elements of approximately equal area (see Piskunov & Kochukhov 2002) using bilinear interpolation.

The change in the geometry slightly reduced the root-mean-square (RMS) values of the magnetic field components as small structures especially at high latitudes were smoothed. Otherwise, the pre-processing did not significantly alter the field topology, except for the filling of the regions around the rotation poles.

The parameters for the pre-processed simulated magnetic field data are listed in Table 1. The magnetic field is characterised by the RMS-values of the total, radial, meridional and azimuthal field ($B_{\rm RMS}$, $B^r_{\rm RMS}$, $B^\theta_{\rm RMS}$ and $B^\phi_{\rm RMS}$). The magnetic field topology is characterised by the percentages of the poloidal ($p_{\rm pol}$) and axi-symmetric ($p_{\rm axi}$) components in terms of magnetic energy. In addition to the original simulations we also used spherical harmonics decompositions reconstructed to the same $\ell_{\rm max} = 20$ as used in most of the ZDI inversions. This data was pre-processed in the same way as the original simulations. For these, we only list the RMS value of the total field in Tab. 1. The input magnetic field data are plotted in Fig. 1.

4. Simulated observations and ZDI setup

Synthetic Stokes IV spectropolarimetric observations were calculated for the three different MHD simulations using a set of different rotation velocities $\upsilon \sin i$, inclinations i and signal-to noise S/N values. For all three maps we initially tested reconstruction with both $n_\phi = 10$ and $n_\phi = 20$ rotation phases evenly distributed between 0 and 1. We also tested the impact of noise by using $S/N = 10^4, 5\cdot10^4$ and 10^5. For the C1 map, we noticed significant differences when using only 10 phases and the lowest S/N compared to the denser phase grid and highest S/N. Thus the final calculations were done with the higher values. For the tests with the H^a and L^a we used $n_\phi = 10$ and $S/N = 10^4$, except when testing different i-values. The $\upsilon \sin i$-range for the C1 reconstruction differed slightly to the other ones, since C1 represents a more slowly rotating case. The effect of i was tested only for the L^a simulation. This choice was based on, that L^a represents the most rapidly rotating model, meaning that this would be the most optimal for ZDI. In order to reduce the influence of random errors, we used $S/N = 5\cdot10^4$ for these cases.

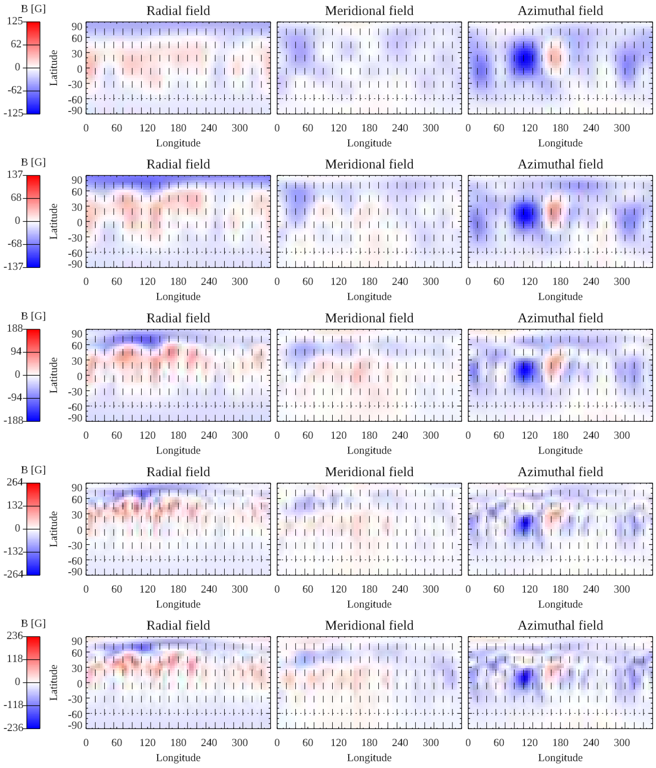

Fig. 2. Resulting ZDI for Tests 1–5 using simulation C1. Top to fourth row: increase of $\upsilon \sin i$ (5, 10, 20 and 40 km s^{-1}), bottom row: $\ell \leq 20$ input. The vertical lines mark the rotational phases of the simulated spectra. The horizontal line marks the visibility limit due to the rotational axis inclination i.

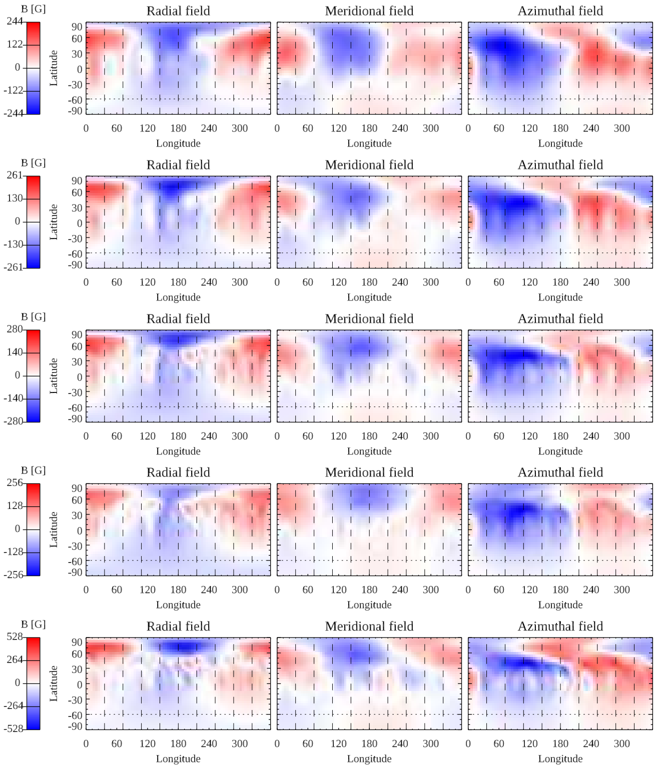

Fig. 3. Resulting ZDI for Tests 6–10 using simulation H^a and $\upsilon \sin i$-values 10, 20, 40 and 60 km s^{-1}. Otherwise same as in Fig. 2.

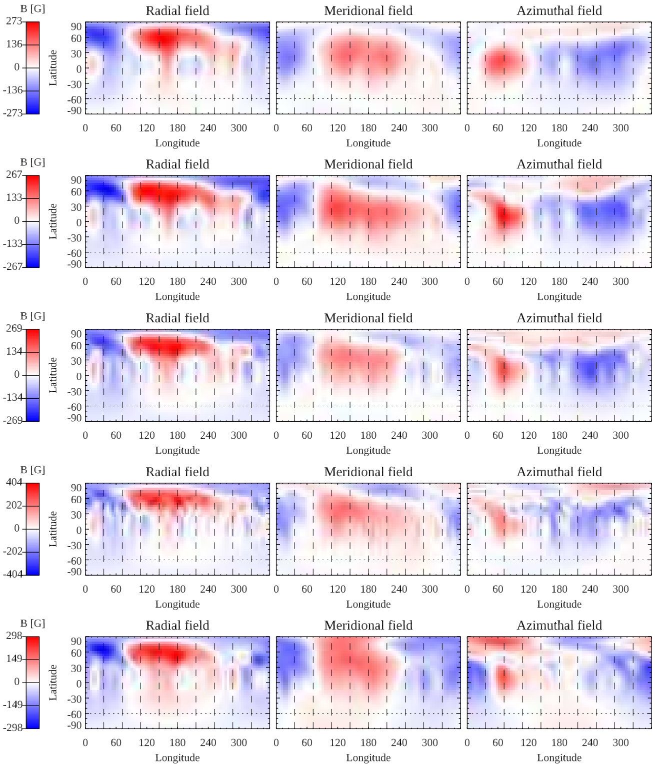

Fig. 4. Resulting ZDI for Tests 11–15 using simulation L^a. Otherwise same as in Fig. 3.

The synthetic Stokes IV profiles were calculated using the same procedure as in Hackman et al. (2016). The intrinsic spectral line width was set to 3 km s^{-1}. This is a combination of both the physical FWHM of the local line profile and the spectral resolution, and would correspond to a spectral resolution of $R \sim 100000$.

Two different values for $\ell_{\max}$ were tested. For $\upsilon \sin i \leq 20$ km s^{-1} $\ell_{\max} = 20$ was found to be sufficient as the contribution from degrees $\ell > 20$ was negligible. For $\upsilon \sin i \geq 40$ km s^{-1} this was not the case, and we adopted a higher value of $\ell_{\max} = 30$. The effect of $\ell_{\max}$ was further explored, by decomposing the original MHD data to degrees $\ell \leq 20$ and running these through the ZDI-reconstruction. These data are labelled C1$_{\ell\leq20}$, H$^a_{\ell\leq20}$ and L$^a_{\ell\leq20}$. Here we only tested the ZDI reconstruction with $\upsilon \sin i$=40 km s^{-1} and $i = 60°$.

The regularisation of the ZDI inversion was done in the same way as described in Rosén et al. (2016). Higher degrees of ℓ were penalised using the regularisation function

$$R = \Lambda \Sigma_{\ell,m} \ell^n (\alpha^2_{\ell,m} + \beta^2_{\ell,m} + \gamma^2_{\ell,m}), \tag{1}$$

where $\alpha_{\ell,m}$, $\beta_{\ell,m}$ and $\gamma_{\ell,m}$ are the harmonic expansion coefficients, m is the azimuthal order and Λ is the regularisation parameter. For the exponent of ℓ in the regularisation, we mostly used the "standard" value $n = 2$ (Tests 1–23 in Tab. 2). For some of the runs we also tried the exponent $n = 1$, in order to explore also this parameter (Tests 24–31).

As no temperature maps were used in the process, we only used the Stokes V profiles for the reconstruction. Magnetic fields will, of course, also alter the Stokes I profiles. But in our cases the magnetic fields were too small to induce any significant effect. This was verified by some initial trials for all three MHD simulations: Inclusion of the Stokes I profiles did not have a no-

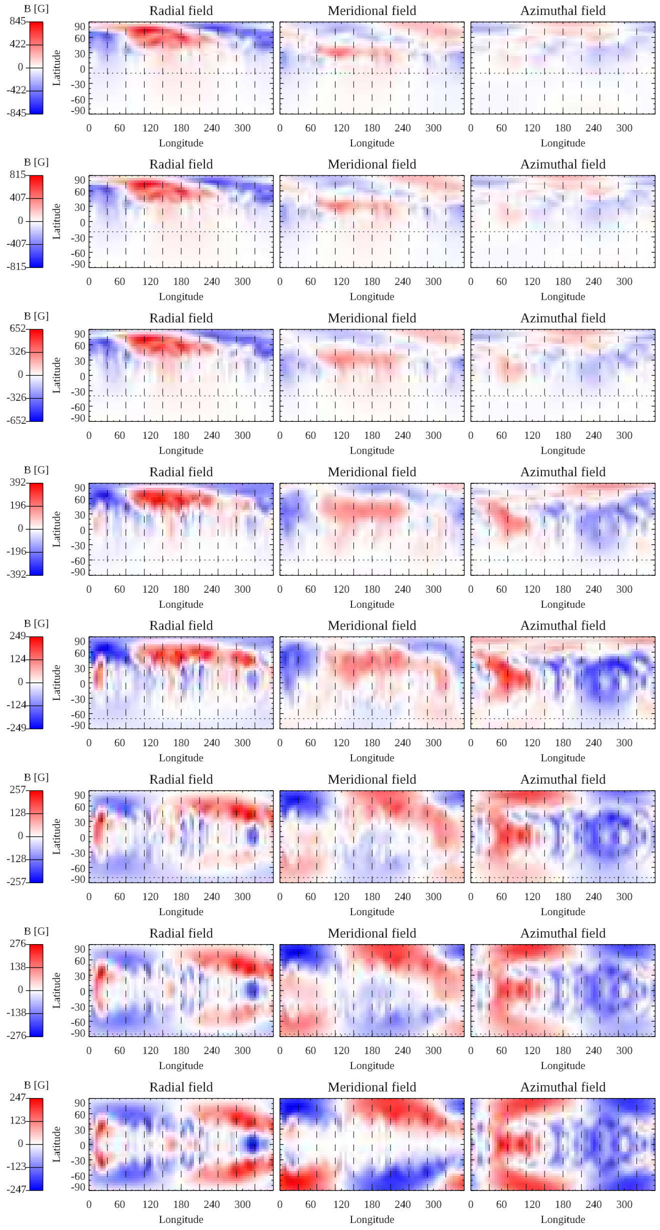

Fig. 5. Resulting ZDI for Tests 16–23 using simulation L^a at variable inclination with constant $v \sin i$=40 km s^{-1}.

table effect on the result in any of these, other than increasing the computation time.

The inversions were started with an initial value of $\Lambda \sim 10^{-7} - 10^{-8}$ (Eq. 1). The value of Λ was gradually reduced, until we reached a χ^2-value of the Stokes V-profiles corresponding to the level of the induced noise in the synthetic data. With real observations, aiming at a reduced $\chi^2 \sim 1$, is seldom a reasonable approach. Firstly, modelling of the Stokes I&V spectra will contain systematic errors. Secondly, in the inversion the ℓ-degrees are limited.

The value of $\ell_{\max}$ is equivalent to the surface resolution of the solution. The resolution will be dependent on the projected rotation velocity of the star combined with the intrinsic line profile. The latter will be a combination of the instrumental spectral resolution and local line-broadening in the stellar photosphere. There is, however no straightforward way to estimate a "correct" value for $\ell_{\max}$, as the rotational resolution varies with the latitude combined with the inclination i. Furthermore, the rotational phase coverage will also play a role, not to mention the S/N. The usual way to set $\ell_{\max}$ is to try out different values, and check at which ℓ-value the remaining magnetic field energy starts to become negligible. Also with synthetic data there is a problem, as the forward modelling does not limit the ℓ-degrees. This naturally becomes a bigger problem when the projected rotation velocity increases, and the theoretical image resolution increases. However, we defend the applied approach with, that it is hard to argue for any other specific target for the reduced χ^2. With real observations one can use a pragmatic approach, and stop the inversions at a level where the decrease in χ^2 reaches a flat stage as a function of decreasing Λ (Kochukhov 2017).

5. Results and discussion

The results are listed in Table 2 and the ZDI maps plotted in Figs. 2 – 5. In addition to the tests listed in the table, we experimented with different values of S/N, $\ell_{\max}$, n_ϕ and the exponent n of the regularisation function (Eq. 1). The results of these are mostly not reported in this study, as they were rather used for choosing reasonable values for the different parameters.

In order to illustrate the effect of $v \sin i$, we plot the retrieved B_{RMS}, axi-symmetry p_{axi} and poloidality p_{pol} as functions of this. We also plot the dependence between the B_{RMS}, axi-symmetry and poloidality (Figs. 6 – 8). In Figs. 9 and 10 we display the dependence of the magnetic field characteristics on the inclination i for the L^a-run using two different values of the exponent n in Eq. 1: $n = 1$ and $n = 2$. For two representative cases ($v \sin i$= 10 km s^{-1} and 40 km s^{-1}) of each MHD simulation we compared the energy distributions as functions of ℓ for the original image and ZDI reconstruction (Figs. 11 – 16).

We only plot the modelled Stokes I and V spectra for three cases, one from each MHD simulation (Fig. 17). This is mainly because all runs were continued until the reduced χ^2-value corresponded to the level of the induced noise in the synthetic Stokes V data. Thus, in all cases the spectra from the ZDI solution will fall into the noise limit of the forward calculated synthetic spectra.

In general, it is clear that the magnetic energy is always lower in the ZDI images than in the original MHD simulations. This is evident both from visually comparing the original images with the ZDI solutions, comparing the RMS values in Tables 1–2, and from the magnetic energy distribution as a function of ℓ-degree (Fig. 11). The percentage of the reconstructed B_{RMS} varied between 18–27% for the C1 case, 26–31% for H^a and 23–42 % for L^a. This reflects the fact, that a considerable part of the magnetic field energy is "hidden" in small structures, i.e. high ℓ-degrees. This fact is also seen in the runs where the ℓ-degrees were already limited in the input data. B_{RMS} is already considerably reduced at this point (see Tab 1).

The biggest difference, when constraining the ℓ degrees already in the input data, is seen in the case of $H^a_{l\leq 20}$, where the reconstructed ZDI has a larger B_{RMS} than those calculated from the H^a data. Otherwise, the reconstructions of the $C1_{l\leq 20}$, $H^a_{l\leq 20}$, and $L^a_{l\leq 20}$ data look quite similar to the corresponding ZDIs from the C1, H^a and L^a data (compare the two bottom panels in Fig. 2 and the bottom panels with the third panels from the top in Figs. 3–4).

There will always be artifacts in the reconstructed field, and these will contribute to RMS values of the total field and its components. Thus the percentages above cannot as such be used as a diagnostic for the reliability of the ZDI inversion. This is demonstrated by the fact, that the optimal values of the inclination, i.e. $i \sim 60 - 70°$ coincide with a minimum of B_{RMS} in the

Table 2. Parameters and results of ZDI inversions: Test ID, MHD simulation, exponent of regularisation function, number of rotational phases, signal-to-noise ratio, projected rotation velocity at equator, inclination of rotation axis, RMS values of the magnetic field, percentages of poloidal and axi-symmetric field energies.

ID	Data	n	n_ϕ	S/N	$v \sin i$ [km s^{-1}]	i [°]	B_{RMS} [kG]	B^r_{RMS} [kG]	B^θ_{RMS} [kG]	B^ϕ_{RMS} [kG]	p_{pol} [%]	p_{axi} [%]
1	C1	2	20	10^5	5	60	0.039	0.013	0.015	0.034	45.4	60.2
2	C1	2	20	10^5	10	60	0.043	0.018	0.014	0.036	50.1	54.2
3	C1	2	20	10^5	20	60	0.051	0.027	0.016	0.040	58.3	50.5
4	C1	2	20	10^5	40	60	0.059	0.033	0.019	0.045	61.2	39.1
5	$\mathrm{C1}_{\ell\leq 20}$	2	20	10^5	40	60	0.058	0.031	0.022	0.044	56.3	45.4
6	H^a	2	10	10^4	10	60	0.129	0.062	0.059	0.096	68.9	7.5
7	H^a	2	10	10^4	20	60	0.127	0.063	0.049	0.100	74.8	6.6
8	H^a	2	10	10^4	40	60	0.125	0.063	0.053	0.094	72.8	11.6
9	H^a	2	10	10^4	60	60	0.148	0.076	0.060	0.112	69.7	13.7
10	$\mathrm{H}^a_{\ell\leq 20}$	2	10	10^4	40	60	0.187	0.084	0.074	0.150	79.2	1.2
11	L^a	2	10	10^4	10	60	0.115	0.069	0.064	0.066	71.5	8.2
12	L^a	2	10	10^4	20	60	0.135	0.080	0.080	0.074	73.6	11.1
13	L^a	2	10	10^4	40	60	0.110	0.068	0.055	0.066	73.0	12.9
14	L^a	2	10	10^4	60	60	0.141	0.087	0.083	0.073	69.8	13.5
15	$\mathrm{L}^a_{\ell\leq 20}$	2	10	10^4	40	60	0.115	0.073	0.059	0.067	65.6	21.3
16	L^a	2	10	$5 \cdot 10^4$	40	10	0.203	0.162	0.105	0.060	82.6	6.6
17	L^a	2	10	$5 \cdot 10^4$	40	20	0.201	0.159	0.104	0.065	82.1	6.2
18	L^a	2	10	$5 \cdot 10^4$	40	40	0.178	0.135	0.093	0.071	79.9	5.9
19	L^a	2	10	$5 \cdot 10^4$	40	60	0.140	0.090	0.074	0.078	73.4	7.6
20	L^a	2	10	$5 \cdot 10^4$	40	70	0.121	0.068	0.058	0.081	75.3	10.0
21	L^a	2	10	$5 \cdot 10^4$	40	80	0.125	0.067	0.061	0.086	77.7	10.3
22	L^a	2	10	$5 \cdot 10^4$	40	85	0.140	0.076	0.075	0.090	76.0	7.4
23	L^a	2	10	$5 \cdot 10^4$	40	90	0.148	0.082	0.081	0.093	75.4	5.2
24	L^a	1	10	$5 \cdot 10^4$	40	10	0.175	0.145	0.086	0.046	85.6	7.3
25	L^a	1	10	$5 \cdot 10^4$	40	20	0.176	0.145	0.083	0.053	85.0	6.8
26	L^a	1	10	$5 \cdot 10^4$	40	40	0.160	0.129	0.072	0.062	83.8	6.1
27	L^a	1	10	$5 \cdot 10^4$	40	60	0.127	0.087	0.059	0.072	77.4	8.0
28	L^a	1	10	$5 \cdot 10^4$	40	70	0.110	0.063	0.047	0.076	75.2	10.3
29	L^a	1	10	$5 \cdot 10^4$	40	80	0.111	0.060	0.048	0.080	74.2	9.1
30	L^a	1	10	$5 \cdot 10^4$	40	85	0.119	0.067	0.055	0.081	74.7	7.2
31	L^a	1	10	$5 \cdot 10^4$	40	90	0.123	0.072	0.060	0.081	74.8	6.4

ZDI (Fig. 10). The sources of such artifacts are limited visibility (especially at low values of i) and symmetry effects (especially at $i \geq 80°$).

The percentages of recovered magnetic field energy show a clear bias towards the lowest ℓ-degrees. This tendency is naturally more accentuated in cases with lower $v \sin i$ and thus poorer spacial resolution. However, as is shown in Fig. 11, the ZDI inversion does not fully recover the field energies even in the lowest ℓ-orders, except for the overestimated energy in $\ell = 1$ in the cases of H^a and H^a. The latter excesses are clearly caused by artifacts in the reconstruction.

The axi-symmetry is generally overestimated. However, our tests show that a more axi-symmetric input field (C1) in general also yields a more axi-symmetric reconstruction. The fraction of the poloidal field energy seems to be better reconstructed. However, we cannot confirm how well trends in the poloidality are reproduced, as all our cases had similar amounts of poloidal field energy.

By visual comparison of the original and ZDI reconstructed images, it is clear that the radial field is best reproduced in all cases. Some of the main structures of the azimuthal field are also captured in the ZDI inversions. Such are e.g. the alternating tilted positive and negative field stripes in the H^a image and the strong negative spot at longitude 120° in C1. The meridional field is generally poorly reproduced. These tendencies are well known consequences of using only Stokes V, but not Q and U (see e.g. Rosén et al. 2015). In general the L^a simulation is best recovered. E.g. the tilt of the high latitude stripes in B^r are well reproduced even with a low $v \sin i$ in the case of L^a compared with the similar feature of H^a.

Naturally, the inversion is also dependent on the inclination i and rotational velocity $v \sin i$. Here the best visual resemblance is achieved with the combination $i \sim 60°$ and $v \sin i \geq 40$ km s^{-1}. With $i \geq 80°$ strong artifacts due to equatorial symmetry will appear in the ZDI maps (Fig. 5, the three panels from the bottom). With $i < 40°$ increasing parts of the stellar surface will be invisible. In fact, our calculations demonstrate the difficulties in reliably recovering the part of the stellar hemisphere below the equator with any value of i. In our cases, the fact that the original data are quite symmetric with respect to the equator will pose extra problems in this respect. In the case of less equatorial symmetry and strong magnetic field structures on the southern hemisphere, these would be better resolved.

The dependence on i explored for the L^a case shows interesting tendencies (Fig. 9). There is clear minimum of B_{RMS} at $i = 70°$ and a maximum of p_{axi} at $i = 80°$. The inclination

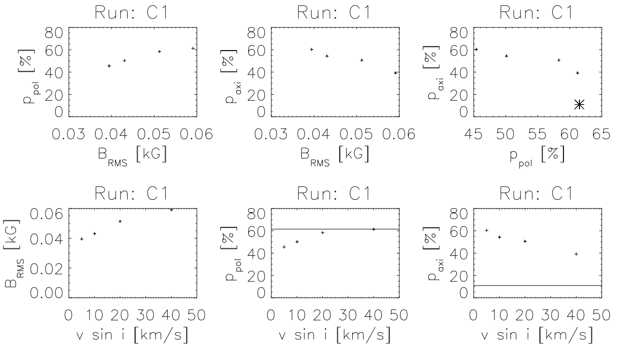

Fig. 6. Results for Tests 1–4 using the simulation C1 showing dependencies of magnetic field characteristics and $\upsilon \sin i$. The asterisk and vertical lines mark the original values.

will especially influence the amount of the meridional and azimuthal field components. This is clearly illustrated as an increasing $B^{\phi}_{\rm RMS}$ and decreasing $B^{\theta}_{\rm RMS}$ with increasing i (Fig. 10). The natural explanation is how these components contribute to the "observed" longitudinal field with different values of i.

Figs. 6–8 illustrate that there are clear dependencies between the reconstructed $B_{\rm rms}$, $p_{\rm pol}$ and $p_{\rm axi}$. In particular, there are correlations between $\upsilon \sin i$ and $p_{\rm axi}$ in all cases. This was seen in all ZDI reconstructions, also the ones used for testing different values of S/N, $\ell_{\rm max}$, n_{ϕ} and not reported here. For the C1 case, all three characteristic ($B_{\rm RMS}$, $p_{\rm pol}$ and $p_{\rm axi}$) of the surface magnetic field are clearly correlated (Fig. 6). This implies that the spurious correlations are stronger, as the Stokes V signal is decreased and the ZDI reconstruction becomes less reliable.

Fig. 16 shows the cumulative fractions of the poloidal and axi-symmetric magnetic energies. These plots show how the summed fractions change with increasing ℓ degree. The plots reveal clear differences between the MHD-simulations. In the cases of H^a and L^a the fractions of poloidal and non-axisymmetric field energies are quite constant, while in the C1 case these fractions increase strongly with larger degrees of ℓ. We also note, that the cumulative function of the fractions are similar both in the original input data and the resulting ZDI solutions. These are also similar for the cases of different $\upsilon \sin i$ values. Furthermore, the cumulative functions for the C1 case resemble those calculated for the Sun by Vidotto (2016).

In the C1 case the higher $\upsilon \sin i$-values yield more reliable images in terms of $p_{\rm pol}$ and $p_{\rm axi}$ (Fig. 6). This tendency is not that clear for H^a and L^a. In these cases a smaller fraction of the magnetic energy is contained in the higher ℓ-degrees (Fig. 11). Thus, a lower $\upsilon \sin i$ will provide a more sufficient resolution. Furthermore, for the H^a and L^a data, the cumulative fractions of poloidal and axi-symmetric magnetic field energy are more constant with ℓ (Fig. 16).

The use of different exponents n in the regularisation (Eq. 1) did not significantly influence the results. This is clear from comparing the indicators ($B_{\rm RMS}$, $B^{r}_{\rm RMS}$, $B^{\theta}_{\rm RMS}$, $B^{\phi}_{\rm RMS}$, $p_{\rm pol}$ and $p_{\rm axi}$) of Tests 16–23 (n = 2) with Tests 24–31 (n = 1) in Table 2 and Figs. 9 – 10. Naturally using the lower n-value led to a marginal increase in the magnetic field energy of higher ℓ-degrees. But the difference in e.g. the distribution of magnetic energy was insignificant.

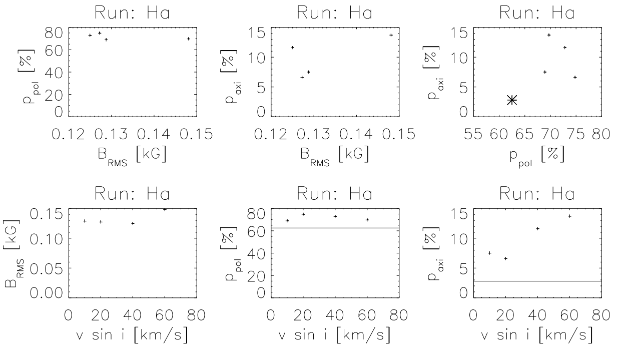

Fig. 7. Results for Tests 6–9 using the simulation H^a. Markings the same as in Fig. 6..

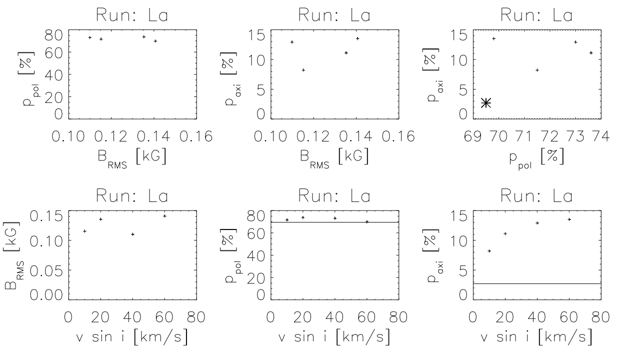

Fig. 8. Results for Tests 11–14 using the simulation L^a. Markings the same as in Fig. 6.

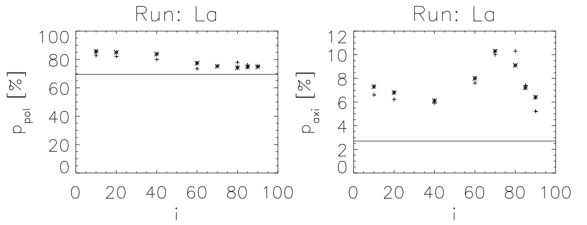

Fig. 9. Effect of inclination on the fractions of poloidal and axisymmetric field energies. The crosses are for Tests 16–23 (n = 2) and the asterisks for Tests 24–31 (n = 1).

6. Conclusions

We have tested the ZDI inversion method by calculating synthetic Stokes IV LSD profiles for a set of MHD simulations from Viviani et al. (2018). We demonstrate, that the reconstructions are dependent on stellar parameters such as the inclination i of the rotational axis. Furthermore, we show that the axi-symmetry of the surface field is in general overestimated in the ZDI images, although the general trend seems to be right. The total field is in turn underestimated due to insufficient resolution. The energy distribution between the poloidal and toroidal field seems to be better reproduced.

Not surprisingly, our study demonstrates the problem of unequal recovering the field components. Using only Stokes V the B^r component will be much more reliably mapped than B^{ϕ} and B^{θ}. The recovery of the latter ones will also depend on the rotational axis inclination i.

The inclination is a particularly problematic parameter in ZDI, as it is usually hard to determine accurately from obser-

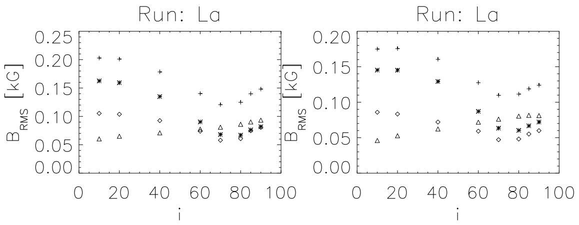

Fig. 10. Effect of inclination on the RMS values of the magnetic field. The left panel is for Tests 16–23 ($n = 2$) and the right panel for Tests 24–31 ($n = 1$). The total field is plotted with crosses, the radial field with asterisks, the merdional field with diamonds and the azimuthal field with triangles.

vations. Furthermore, the range of optimal values of i is narrow. With $i < 40°$ a large part of the star will be hidden, hampering conclusions of the magnetic field topology. With $i > 80°$ there will be problems with equatorial symmetry.

The retrieved field distribution in terms of the angular degree ℓ can generally not be trusted. There is a clear transition from higher degrees in the original field to lower degrees in the reconstruction. This can partly be understood as a blurring effect in the ZDI inversion. Furthermore, we note that limiting the angular degrees to too small values may be problematic. This is very evident for the C1 data, which represents a less active star. Lehmann et al. (2019) recommended that $\ell_{\max} = 5$ would be enough for less active slow rotators. This is true in the sense, that with a $\upsilon \sin i \sim 10$ km s^{-1}, the spacial resolution will usually not be enough to resolve details of $\ell > 5$. However, our results indicate, that a large fraction of the the magnetic energy is in the higher ℓ-degrees for less active stars. As the relation between the optimal $\ell_{\max}$ and $\upsilon \sin i$ is not trivial, we would recommend using a higher $\ell_{\max} \sim 10$–20, even for slow rotators.

Although the magnetic field energy in specific ℓ degrees cannot be trusted, the cumulative distribution of the fractions of poloidal vs. toroidal and axi-symmetric vs. non-axisymmetric field energy are surprisingly well reproduced. Again the C1 data, differed from the two other cases, in that the cumulative distribution changed significantly as a function of ℓ. However, this change was similar in both the original data and the ZDI reconstructions.

The above mentioned discrepancies can be seen as a critique against how ZDI results are sometimes reported. It is somewhat problematic to compare the magnetic topology of different stars, without accounting for systematic biases related to stellar parameters. Here, the impact of the inclination has usually been neglected in ZDI studies.

Our study also emphasises the importance of high quality observations. With a weaker field (C1 in our study), there is a need of extremely high S/N and dense phase coverage, in addition to the high spectral resolution. Perhaps a more surprising result is that the quality of the reconstruction is not that dependent on the rotation velocity. Even low $\upsilon \sin i$-values (≤ 10 km s^{-1}) may allow for reasonable reconstruction. The $\upsilon \sin i$-values will, of course, be more important if temperature mapping using Stokes I is included.

Acknowledgements. This work received funding from the Academy of Finland (project SOLSTICE, decision No. 324161). O.K. acknowledges support by the Swedish Research Council (grant agreement no. 2019-03548), the Swedish National Space Agency, and the Royal Swedish Academy of Sciences. This project has received funding from the European Research Council (ERC) under the European Union's Horizon 2020 research and innovation program (Project UniSDyn, grant agreement n:o 818665). This work was done in collaboration with the COFFIES DRIVE Science Center.

References

Brown, S. F., Donati, J. F., Rees, D. E., & Semel, M. 1991, A&A, 250, 463
Donati, J. F., Howarth, I. D., Jardine, M. M., et al. 2006, MNRAS, 370, 629
Donati, J. F., Morin, J., Petit, P., et al. 2008, MNRAS, 390, 545
Donati, J. F., Semel, M., Carter, B. D., Rees, D. E., & Collier Cameron, A. 1997, MNRAS, 291, 658
Gibb, G. P. S., Mackay, D. H., Jardine, M. M., & Yeates, A. R. 2016, MNRAS, 456, 3624
Hackman, T., Lehtinen, J., Rosén, L., Kochukhov, O., & Käpylä, M. J. 2016, A&A, 587, A28
Käpylä, P. J., Mantere, M. J., Cole, E., Warnecke, J., & Brandenburg, A. 2013, ApJ, 778, 41
Kochukhov, O. 2015, A&A, 580, A39
Kochukhov, O. 2016, in Lecture Notes in Physics, Berlin Springer Verlag, ed. J.-P. Rozelot & C. Neiner, Vol. 914, 177
Kochukhov, O. 2017, A&A, 597, A58
Kochukhov, O., Lüftinger, T., Neiner, C., Alecian, E., & MiMeS Collaboration. 2014, A&A, 565, A83
Kochukhov, O., Mantere, M. J., Hackman, T., & Ilyin, I. 2013, A&A, 550, A84
Landi Degl'Innocenti, E. & Landolfi, M. 2004, Astrophysics and Space Science Library, Vol. 307, Polarization in Spectral Lines (Kluwer Academic Publishers)
Lehmann, L. T., Hussain, G. A. J., Jardine, M. M., Mackay, D. H., & Vidotto, A. A. 2019, MNRAS, 483, 5246
Lehmann, L. T., Jardine, M. M., Mackay, D. H., & Vidotto, A. A. 2018, MNRAS, 478, 4390
Pencil Code Collaboration, Brandenburg, A., Johansen, A., et al. 2021, The Journal of Open Source Software, 6, 2807
Piskunov, N. & Kochukhov, O. 2002, A&A, 381, 736
Rosén, L., Kochukhov, O., Hackman, T., & Lehtinen, J. 2016, A&A, 593, A35
Rosén, L., Kochukhov, O., & Wade, G. A. 2015, ApJ, 805, 169
Vidotto, A. A. 2016, MNRAS, 459, 1533
Viviani, M., Käpylä, M. J., Warnecke, J., Käpylä, P. J., & Rheinhardt, M. 2019, ApJ, 886, 21
Viviani, M., Warnecke, J., Käpylä, M. J., et al. 2018, A&A, 616, A160
Willamo, T., Lehtinen, J. J., Hackman, T., et al. 2022, A&A, 659, A71

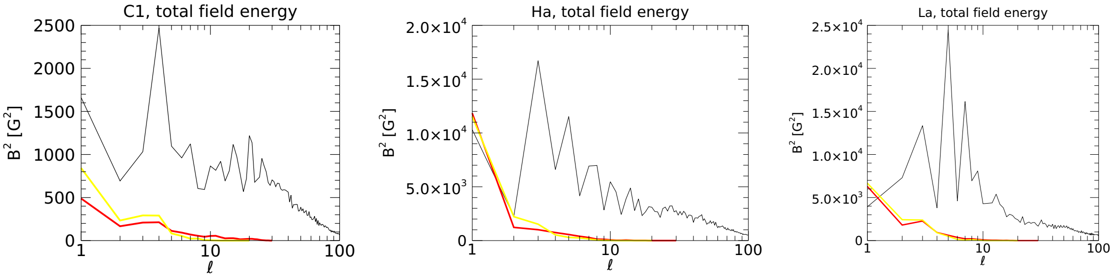

Fig. 11. Contribution to the mean magnetic energy by ℓ-degrees: Original images (black line); Tests 2, 6 and 11 ($\upsilon \sin i$= 10 km s^{-1}, yellow line); Tests 4, 8 and 13 ($\upsilon \sin i$= 40 km s^{-1}, red line).

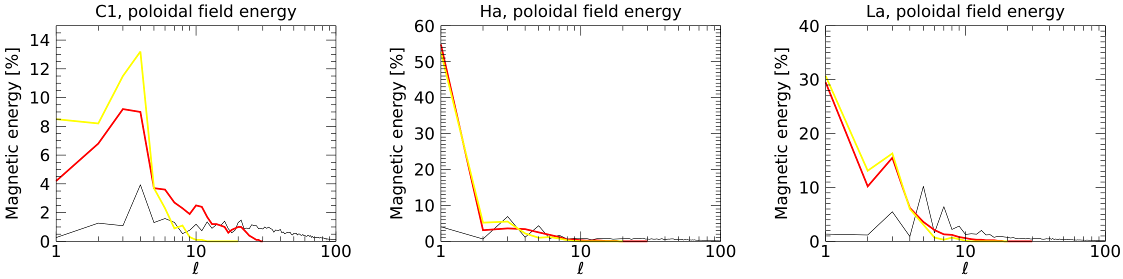

Fig. 12. Poloidal fraction the magnetic energy by ℓ-degrees. Colour markings the same as in Fig. 11.

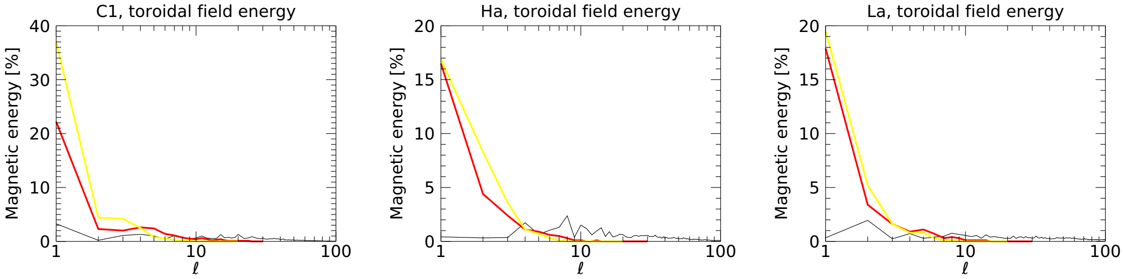

Fig. 13. Toroidal fraction of the magnetic energy by ℓ-degrees. Colour markings the same as in Fig. 11.

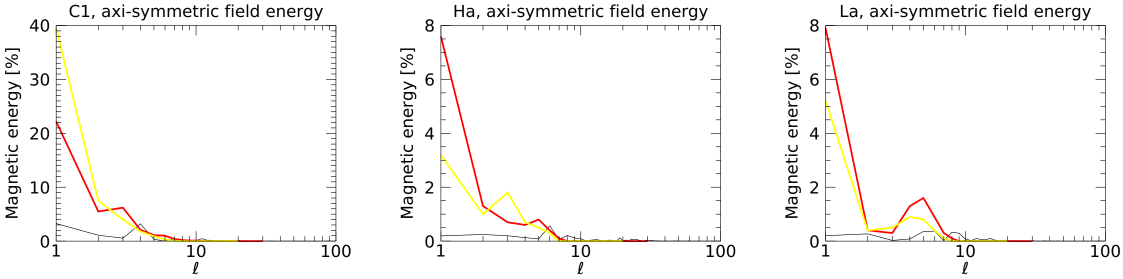

Fig. 14. Axi-symmetric fraction of the magnetic energy by ℓ-degrees. Colour markings the same as in Fig. 11.

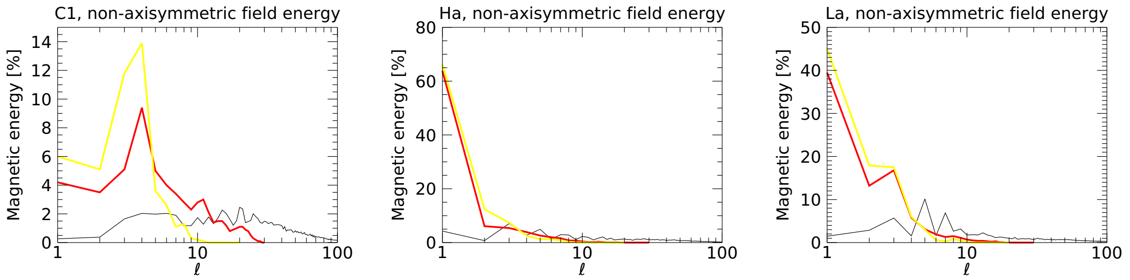

Fig. 15. Non-axisymmetric fraction of the magnetic energy by ℓ-degrees. Colour markings the same as in Fig. 11.

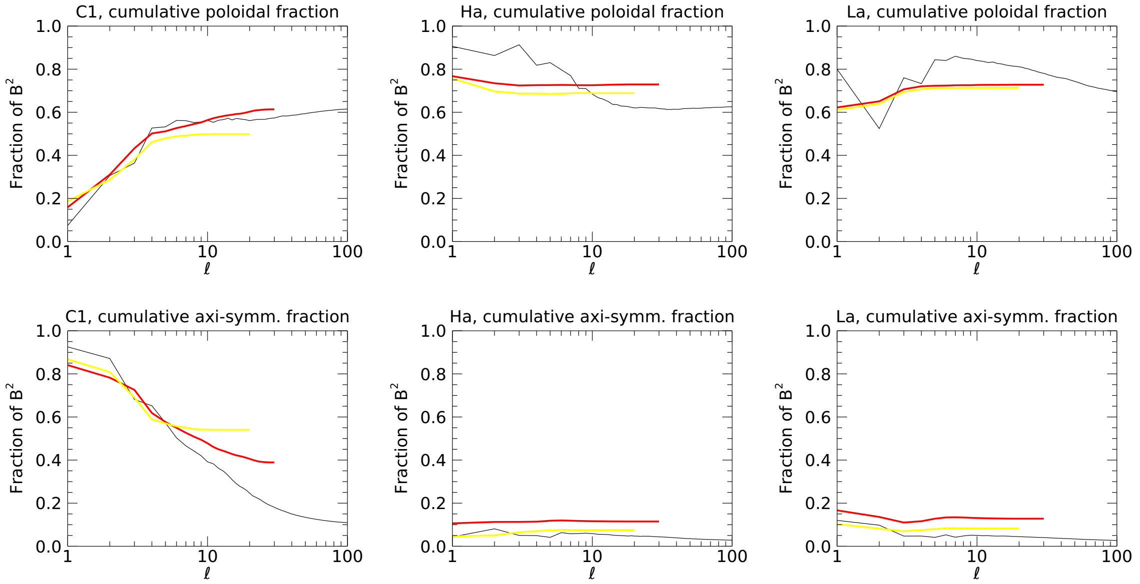

Fig. 16. Cumulative fractions of the magnetic energy by ℓ-degrees. Colour markings the same as in Fig. 11.

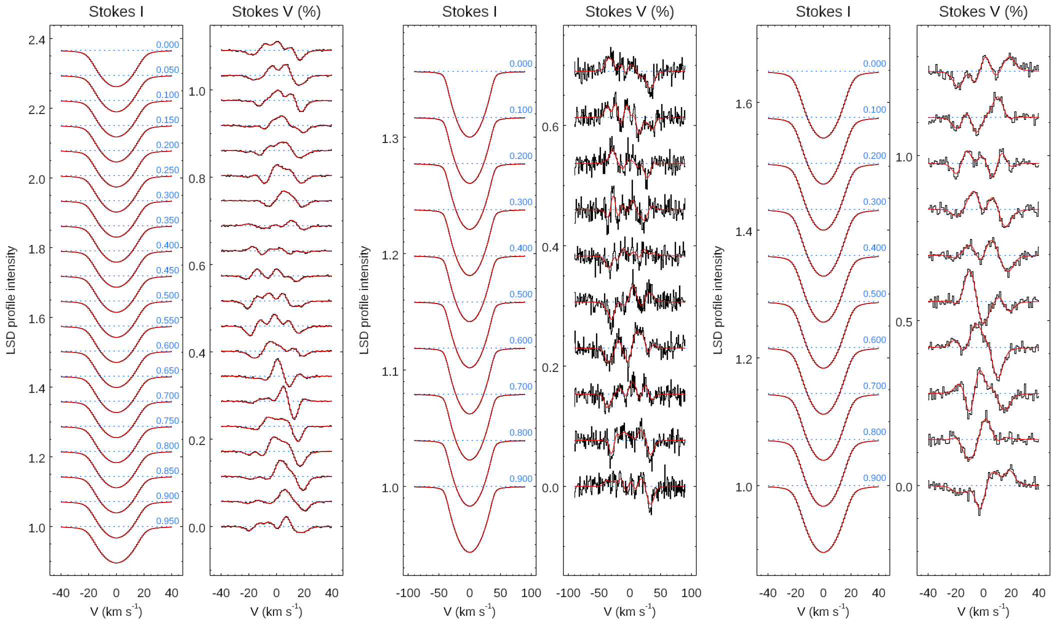

Fig. 17. Simulated (black) and calculated (red) profiles for Tests 3, 7 and 12.